

4-2009

Drive-Mode Control for Vibrational MEMS Gyroscopes


Lili Dong

Cleveland State University, l.dong34@csuohio.edu

David Avanesian

Cleveland State University

Follow this and additional works at: https://engagedscholarship.csuohio.edu/enece_facpub

 Part of the [Controls and Control Theory Commons](#), and the [Electronic Devices and Semiconductor Manufacturing Commons](#)

How does access to this work benefit you? Let us know!

Original Citation

Lili, D., & Avanesian, D. (2009). Drive-mode control for vibrational MEMS gyroscopes. *IEEE Transactions on Industrial Electronics*, 56, 4, 956-963.

Repository Citation

Dong, Lili and Avanesian, David, "Drive-Mode Control for Vibrational MEMS Gyroscopes" (2009). *Electrical Engineering and Computer Science Faculty Publications*. 102.
https://engagedscholarship.csuohio.edu/enece_facpub/102

This Article is brought to you for free and open access by the Electrical and Computer Engineering Department at EngagedScholarship@CSU. It has been accepted for inclusion in Electrical Engineering and Computer Science Faculty Publications by an authorized administrator of EngagedScholarship@CSU. For more information, please contact library.es@csuohio.edu.

Drive-Mode Control for Vibrational MEMS Gyroscopes

Lili Dong, *Member, IEEE*, and David Avanesian, *Student Member, IEEE*

Abstract—This paper presents a novel design methodology and hardware implementation for the drive-mode control of vibrational micro-electro-mechanical systems gyroscopes. Assuming that the sense mode (axis) of the gyroscope is operating under open loop, the drive-mode controller compensates an undesirable mechanical spring-coupling term between the two vibrating modes, attenuates the effect of mechanical–thermal noise, and most importantly, forces the output of the drive mode to oscillate along a desired trajectory. The stability and robustness of the control system are successfully justified through frequency-domain analysis. The tracking error between the real output and the reference signal for the drive mode is proved to be converging with the increase of the bandwidth of the controller. The controller is first simulated and then implemented using field-programmable analog array circuits on a vibrational piezoelectric beam gyroscope. The simulation and experimental results verified the effectiveness of the controller.

Index Terms—Analog implementation, drive-mode control, micro-electro-mechanical systems (MEMS), vibrational gyroscopes.

I. INTRODUCTION

MICRO-ELECTRO-MECHANICAL systems (MEMS) gyroscopes are silicon micromachined vibrational gyroscopes that are used to measure rotation rates. The main benefits of the MEMS gyroscopes are “mass production,” “low cost,” and “monolithic integration” [1]. These advantages have offered MEMS gyroscopes broad applications in automobiles (rollover detection and navigation), consumer electronics (angular detection for 3-D mouse and image stabilization for video camera), spacecraft (homing and GPS-assisted navigation), robotics, and some military uses [2]. The parameters of ideal MEMS gyroscopes such as natural frequency, damping coefficient, and mass are fixed, the vibrations along two axes of the gyroscope are mechanically uncoupled, and the gyroscope is only sensitive to the rotation rate but not to noise. However, in real-world situations,

fabrication imperfection and environmental variations cause parameter changes, mechanical couplings between two axes, and mechanical–thermal noises along the axes, which will greatly degrade the sensitivity of the gyroscope.

In the past 20 years, researchers have been focusing on developing advanced control electronics to compensate the fabrication imperfections and improve the performance of the MEMS gyroscopes. Most of the reported controllers are based on accurate model information of the MEMS gyroscopes. The parameter identification and sensor modeling have been introduced in [4]–[6]. A typical phase-locked loop (PLL) [7] is utilized to adjust the input frequency to resonant frequency, and an automatic gain control loop [8] is employed to regulate the output amplitude. In [7] and [8], the input frequency is dependent on the mechanics of device and changes with environmental variations. As an alternative to the PLL control, an adaptive controller [9] is developed to tune the closed-loop frequency of the drive axis to a fixed frequency chosen by the designer. However, in [9], the amplitude regulation of the drive axis is disregarded. In [10], an adaptive oscillation controller is introduced without requiring an external reference signal. Nevertheless, the controller assumed an ideal model of the drive axis and did not consider the mechanical coupling terms between both axes. The research of the adaptive oscillation controller was extended in [11], where two vibrating axes were controlled to sense a constant rotation rate. Since the rotation rate is changing with time in reality, the adaptive controllers for measuring time-varying rates are developed in [12] and [13]. The controllers in [4]–[12] are based on conventional MEMS gyroscopes where only the drive axis of the gyroscope is driven to resonance while the output of the sense axis is regulated to zero. In [13] and [14], an adaptive mode of operation for the MEMS gyroscopes is introduced, in which both vibrating axes are controlled and excited to resonance.

In this paper, we develop a drive-mode controller for the conventional MEMS gyroscope in which the mechanical coupling terms, noise, and parameter variations are all considered. We will apply an active disturbance rejection controller (ADRC) [15]–[20] to excite the drive axis to resonance and to stabilize the magnitude of its output at a fixed value. The controller generalizes the disturbance as any discrepancies between the mathematical model and the actual gyroscope system and actively compensates the disturbance in real time, hence the name ADRC. Since the ADRC does not require accurate model information, it is very robust against the structural uncertainties of the MEMS gyroscope. So far, the ADRC has been successfully applied to macrosystems. In this paper, we modify the controller and extend its use to the MEMS gyroscopes.

This paper is organized as follows. The dynamics of a MEMS gyroscope is explained in Section II. The drive-mode controller is presented in Section III. Simulation results are shown in Section IV. The analog implementation and experimental results are given in Section V. The concluding remarks are made in Section VI.

II. SYSTEM DYNAMICS AND MODELING

A vibrational MEMS gyroscope is consisting of a vibrational proof mass, dampers, springs, and a rigid frame. The rigid frame is rotating about the rotation axis at a rotation rate Ω . The proof mass is excited to oscillate at maximum amplitude along the drive axis (X -axis) containing the springs and dampers. The Coriolis force and mechanical coupling forces transfer the energy from the drive axis to the sense axis (Y -axis), resulting in the vibration along the sense axis. Since the Coriolis force is proportional to the rotation rate, the rate can be approximated from the vibration of the sense axis. In order to precisely approximate the rotation rate (around the rotation axis alone), the primary task of the controller for the MEMS gyroscope is to assure a constant-amplitude oscillation of the drive axis. Since the output signal of the MEMS gyroscope is generally very small, another task of the controller is to force the drive axis to vibrate at resonance so as to achieve the largest response.

We suppose that the sense axis is under open-loop control. Let m denote the inertial mass, x and y the displacement outputs of both axes, and c the controller gain comprising actuator and sensor scale factors. The vibrational MEMS gyroscope is modeled as

$$\ddot{q} + D\dot{q} + Kq + S\dot{q} = BU + CN \quad (1)$$

where $q(t) = [x(t), y(t)]^T \in R^2$ is the displacement output vector of both axes of the gyroscope, $D \in R^{2 \times 2}$ refers to the damping coefficient matrix, $K \in R^{2 \times 2}$ denotes the spring constant matrix, $S \in R^{2 \times 2}$ denotes the Coriolis effect matrix, $S\dot{q}$ are Coriolis accelerations, $B \in R^{2 \times 2}$ is a controller gain matrix, $C \in R^{2 \times 2}$ is a gain matrix for noise input, $U(t) = [u_x(t), 0]^T \in R^2$ is the control input vector, and $N = [N_x, N_y] \in R^2$ is a mechanical-thermal noise vector. The concept of mechanical-thermal noise is originally from the Johnson noise of a resistor in an electrical circuit. As introduced in [21], the power spectral density (PSD) of the thermal noise in a resistor can be represented by

$$S_n(f) = 4K_B T R N^2 s \quad (2)$$

where K_B is a Boltzmann constant ($K_B = 1.38 \times 10^{-23} \text{ JK}^{-1}$), T is the absolute temperature of the resistor, and R is resistance. In real systems, any dissipative process, coupled to a thermal reservoir, can result in thermal noise. In the mechanical model of the MEMS gyroscope, the damper is equivalent to the resistor. Because the PSD is constant over all frequencies, the mechanical-thermal noise is considered as white noise and represented by $(0, S_n)$.

Due to fabrication imperfections, there are two mechanical coupling terms on the drive and sense axes: damping and spring. In this paper, we assume zero damping coupling but only consider the spring-coupling term. Define d_{xx} and d_{yy} as

damping coefficients, k_{xx} and k_{yy} as spring constants, and k_{xy} as the spring-coupling term for both axes. Since the undesirable spring-coupling term is 90° out of phase with the useful Coriolis accelerations, we also call the spring couplings as quadrature errors. The displacement output of drive axis $x(t)$ is usually so large that the effects of thermal noise on the drive axis are negligible and are disregarded [10]. For the conventional MEMS gyroscope, the displacement of the sense axis is very small. It tends to be contaminated by the noise. Therefore, the noise on the sense axis cannot be ignored. Given that the natural frequencies for both axes are matched and the sense axis is under open-loop control, we have

$$\begin{aligned} D &= \begin{bmatrix} \frac{d_{xx}}{m} & 0 \\ 0 & \frac{d_{yy}}{m} \end{bmatrix} & K &= \begin{bmatrix} \frac{k_{xx}}{m} & \frac{k_{xy}}{m} \\ \frac{k_{xy}}{m} & \frac{k_{yy}}{m} \end{bmatrix} \\ B &= \begin{bmatrix} \frac{c}{m} & 0 \\ 0 & 0 \end{bmatrix} & C &= \begin{bmatrix} 0 & 0 \\ 0 & \frac{c}{m} \end{bmatrix} & S &= \begin{bmatrix} 0 & -2\Omega \\ 2\Omega & 0 \end{bmatrix}. \end{aligned} \quad (3)$$

Define $d_{xx}/m = 2\zeta\omega_n$, $k_{xx}/m = \omega_n^2$, and $k_{xy}/m = \omega_{xy}$. Combining (1) and (3), we have

$$\begin{cases} \ddot{x} = -2\zeta\omega_n\dot{x} - \omega_n^2x - \omega_{xy}y + 2\Omega\dot{y} + \frac{c}{m}u_x \\ \ddot{y} = -2\zeta\omega_n\dot{y} - \omega_n^2y - \omega_{xy}x - 2\Omega\dot{x} + \frac{c}{m}N_y. \end{cases} \quad (4)$$

Our control objective is to force the drive axis to oscillate at a specified amplitude and the resonant frequency in the presences of parameter variations, mechanical couplings, and the mechanical-thermal noise.

III. DRIVE-MODE CONTROLLER DESIGN

From (4), the drive-axis model can be rewritten as

$$\ddot{x} = f(x, \dot{x}, d) + bu_x \quad (5)$$

where b is the coefficient of the controller ($b = c/m$), d is an extraneous input force [15], and $f(x, \dot{x}, d)$ (or simply denoted as f) accounts for all the other forces excluding the control effort u_x , which is

$$f = -2\zeta\omega_n\dot{x} - \omega_n^2x - \omega_{xy}y + 2\Omega\dot{y}. \quad (6)$$

We assume that b is known. If an observer is designed to estimate the f , we can take u_x as

$$u_x = \frac{1}{b} \left(-\hat{f}(\dot{x}, x, d) + u_0 \right) \quad (7)$$

where \hat{f} is the estimated f and u_0 is a controller to be determined. Then, (5) becomes

$$\ddot{x} = f(\dot{x}, x, d) - \hat{f}(\dot{x}, x, d) + u_0 \approx u_0. \quad (8)$$

We suppose that a desired signal r has the resonant frequency ω and the maximum amplitude A that the drive axis could output. Moreover, r is represented by

$$r = A \sin(\omega t). \quad (9)$$

Then, our control goal is to drive the output signal x to the signal r . We have tracking error $e = r - x$. We can employ a

common proportional-derivative controller for u_0 to drive the tracking error e to zero. The controller is

$$u_0 = k_p e + k_d \dot{e} + \ddot{r}. \quad (10)$$

If we take the unknown f as a generalized disturbance or the discrepancy between the real system and its nominal model, the controller will estimate it and compensate for it actively.

A. ESO

The effectiveness of the ADRC is dependent on the accurate estimation of the f . Consequently, an extended state observer (ESO) is developed to estimate the disturbance f in real time. This can be achieved by using the linear state space representation of the drive-axis model and augmenting the state variables to include f [16]. It is assumed that the unknown function $f(x, \dot{x}, d)$ is locally Lipschitz in the argument and bounded within the domain of interests. Let $x_1 = x$, $x_2 = \dot{x}$, $x_3 = f$, and $X = [x_1, x_2, x_3]^T$, and we have

$$\begin{aligned} \dot{X} &= AX + Bu_x + Eh \\ Z &= CX \end{aligned} \quad (11)$$

where

$$\begin{aligned} A &= \begin{bmatrix} 0 & 1 & 0 \\ 0 & 0 & 1 \\ 0 & 0 & 0 \end{bmatrix} & B &= \begin{bmatrix} 0 \\ b \\ 0 \end{bmatrix} \\ C &= [1 & 0 & 0] & E &= \begin{bmatrix} 0 \\ 0 \\ 1 \end{bmatrix} & h &= \dot{f}. \end{aligned}$$

Based on (11), a state observer is given by

$$\begin{aligned} \dot{\hat{X}} &= A\hat{X} + Bu_x + L(Z - \hat{Z}) \\ \hat{Z} &= C\hat{X} \end{aligned} \quad (12)$$

where the estimated state vector is $\hat{X} = [\hat{x}_1, \hat{x}_2, \hat{x}_3]^T$ and the vector of observer gain is $L = [l_1, l_2, l_3]^T$. We need to notice that the key part of (12) is the third state of observer \hat{x}_3 , which is used to approximate f . The characteristic polynomial of the observer (12) is represented by

$$p(s) = s^3 + \alpha_1 s^2 + \alpha_2 s + \alpha_3. \quad (13)$$

If the observer gains are selected as $l_1 = 3\omega_o$, $l_2 = 3\omega_o^2$, $l_3 = \omega_o^3$, and $\omega_o > 0$, the characteristic polynomial becomes

$$p(s) = (s + \omega_o)^3. \quad (14)$$

Therefore, we can change the observer gains through tuning the unique parameter ω_o , which is also the bandwidth of the observer.

B. Control Algorithm

Based on (11) and (12), the drive-mode controller (7) becomes

$$u_x = \frac{1}{b}(-\hat{x}_3 + u_0). \quad (15)$$

In order to minimize the number of tuning parameters of the controller u_0 , the controller parameters are chosen as $K_p = \omega_c^2$ and $K_d = 2\omega_c$, where $\omega_c > 0$. Then, (10) becomes

$$u_0 = \omega_c^2 e + 2\omega_c \dot{e} + \ddot{r}. \quad (16)$$

From (15) and (16), we can see that ω_c is the only one tuning parameter for the control input u_x . Since the velocity of the movement along the drive axis is not measurable, the controller u_0 built on the observed velocity is shown as

$$u_0 = \omega_c^2(r - \hat{x}_1) + 2\omega_c(\dot{r} - \hat{x}_2) + \ddot{r}. \quad (17)$$

Assuming accurate estimations of the states by the ESO, the ideal closed-loop transfer function (TF) of the controller is

$$G(s) = \frac{x}{r} = 1 \quad (18)$$

which indicates that we reached our control goal through the drive-mode controller. The details about how to tune the parameters of the ADRC are introduced in [16]. In this paper, we choose $\omega_o = 5\omega_c$.

C. TFR of ADRC

For the sake of analog hardware implementation, a transfer function representation (TFR) of the ADRC is developed in this section. The TFR, which is extensively used by industrial engineers, will also enable stability analysis and evaluation of a steady-state performance of the closed-loop control system for the drive axis of the MEMS gyroscope.

1) *TF Derivation:* The Laplace transform (LT) of (4) for the drive axis is

$$\begin{aligned} x(s) &= \frac{-\omega_{xy}y + 2\Omega(s)s}{s^2 + 2\zeta\omega_n s + \omega_n^2} y(s) + \frac{b}{s^2 + 2\zeta\omega_n s + \omega_n^2} u_x(s) \\ &= d(s) + G_p(s)u_x(s) \end{aligned} \quad (19)$$

where $d(s)$ is taken as the input disturbance to the drive axis and $G_p(s)$ is the TF of the drive axis. The LT of the controller given by (15) and (17) is

$$u_x(s) = \frac{1}{b} \begin{bmatrix} k_p & k_d & 1 \end{bmatrix} \begin{bmatrix} r(s) \\ s r(s) \\ s^2 r(s) \end{bmatrix} - \frac{1}{b} \begin{bmatrix} k_p & k_d & 1 \end{bmatrix} \hat{X}(s). \quad (20)$$

The LT of the ESO represented by (11) and (12) is

$$s\hat{X}(s) = (A - LC)\hat{X}(s) + LZ(s) + Bu_x(s). \quad (21)$$

Replacing the $\hat{X}(s)$ in (20) with (21), we have

$$\begin{aligned} u_x(s) &= \frac{1}{b} \frac{s^3 + l_1 s^2 + l_2 s + l_3}{s^3 + \beta_1 s^2 + \beta_2 s} (k_p + k_d s + s^2) r(s) \\ &\quad - \frac{1}{b} \frac{\mu_1 s^2 + \mu_2 s + \mu_3}{s^3 + \beta_1 s^2 + \beta_2 s} Z(s) \end{aligned} \quad (22)$$

where the coefficients in (22) are listed in Table I.

TABLE I
DEFINITION OF PARAMETERS

$\beta_1 = l_1 + k_d$	$\beta_2 = l_2 + k_p + k_d l_1$
$\mu_1 = k_p l_1 + k_d l_2 + l_3$	$\mu_2 = k_p l_2 + k_d l_3$
$\mu_3 = k_p l_3$	$A_d(s) = s^5 + (2\zeta\omega_n + \beta_1)s^4 + (\omega_n^2 + 2\zeta\omega_n\beta_1 + \beta_2)s^3 + (\beta_1\omega_n^2 + 2\zeta\omega_n\beta_2 + \mu_1)s^2 + (\omega_n^2\beta_2 + \mu_2)s + \mu_3$
$\omega_n = 63881.1 \text{ rad/s}$	$\zeta = 0.0005$
$\omega = 65973.4 \text{ rad/s}$	$b = 271780942.56$
$\omega_{xy} = 6000$	$\Omega = 0.1 \text{ rad/s}$

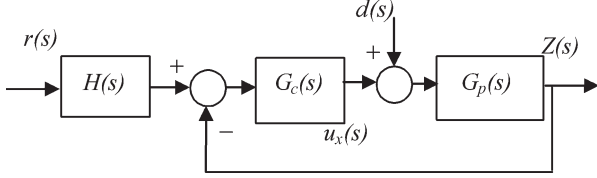


Fig. 1. Block diagram of the closed-loop system in TF form.

Let

$$G_c(s) = \frac{1}{b} \frac{\mu_1 s^2 + \mu_2 s + \mu_3}{s^3 + \beta_1 s^2 + \beta_2 s}$$

$$H(s) = \frac{(s^3 + l_1 s^2 + l_2 s + l_3)(k_p + k_d s + s^2)}{\mu_1 s^2 + \mu_2 s + \mu_3}. \quad (23)$$

Equation (22) can be rewritten as

$$u_x(s) = H(s)G_c(s)r(s) - G_c(s)Z(s). \quad (24)$$

Then, the closed-loop control system for the drive axis is shown in Fig. 1.

From Fig. 1, the open-loop TF is

$$G_o(s) = G_c(s)G_p(s). \quad (25)$$

The closed-loop TF is

$$G_{cl}(s) = \frac{Z(s)}{r(s)} = \frac{H(s)G_c(s)G_p(s)}{1 + G_c(s)G_p(s)}. \quad (26)$$

Furthermore, the TF from the input disturbance to the output is

$$G_d(s) = \frac{Z(s)}{d(s)} = \frac{G_p(s)}{1 + G_c(s)G_p(s)}. \quad (27)$$

2) *Convergence of Tracking Error:* In this paper, we used a piezoelectrically driven vibrational beam gyroscope to evaluate the drive-mode controller. The parameters of the vibrational gyroscope are given in Table I.

As in (9), the reference signal for the drive axis is $r = A \sin(\omega t)$. According to (26), the steady-state output of the drive axis is

$$x_{ss} = A |G_{cl}(j\omega)| \sin(\omega t + \phi) \quad (28)$$

where the phase shift is

$$\phi = \angle G_{cl}(j\omega) = \tan^{-1} \frac{\text{Im}(G_{cl}(j\omega))}{\text{Re}(G_{cl}(j\omega))}. \quad (29)$$

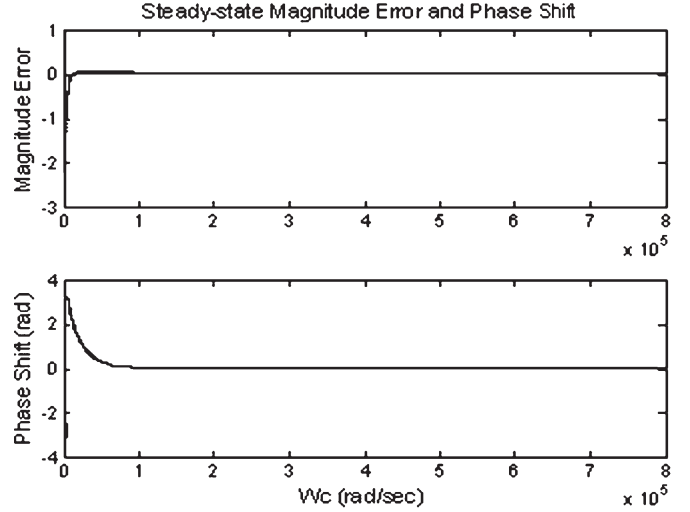


Fig. 2. Steady-state magnitude error and phase shift.

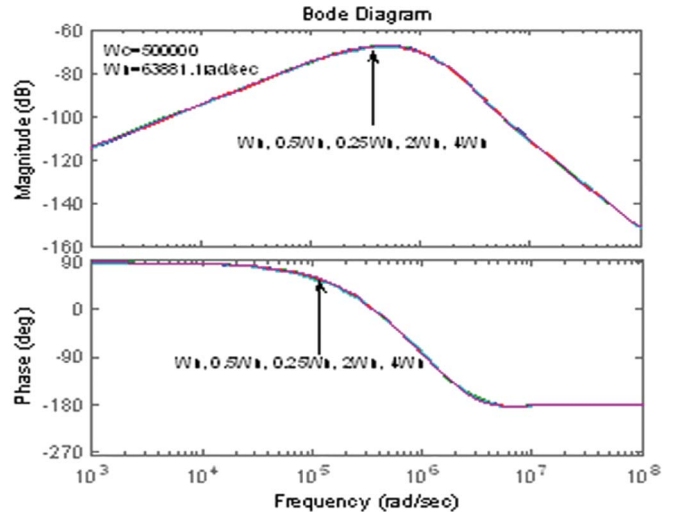


Fig. 3. Bode plots of $G_d(s)$ for different ω_n 's.

Define the magnitude error between the steady-state output of the drive axis and the reference signal as $e_m = A - A|G_{cl}(j\omega)|$. The e_m and Φ versus the controller gain ω_c are shown in Fig. 2, where both the magnitude error and the phase shift of the steady-state output of the drive axis are converging to zeros with the increase of the controller bandwidth ω_c . According to Fig. 2, we choose $\omega_c = 5 \times 10^5$, for which e_m is about 1.6% of the reference magnitude and $\Phi = -0.006$ rad, in the computer simulation and hardware implementation of the ADRC.

3) *External Disturbance Rejection:* This section will show how the external disturbance is rejected by the ADRC in the presence of the structural uncertainties of the vibrational gyroscope. Substituting the $G_p(s)$ in (19) and the $G_c(s)$ in (23) into (27), we have

$$G_d(s) = \frac{bs(s^2 + \beta_1 s + \beta_2)}{A_d(s)} \quad (30)$$

where $A_d(s)$, given in Table I, is a fifth-order polynomial with a nonzero constant term. From (30), we can see that, as the

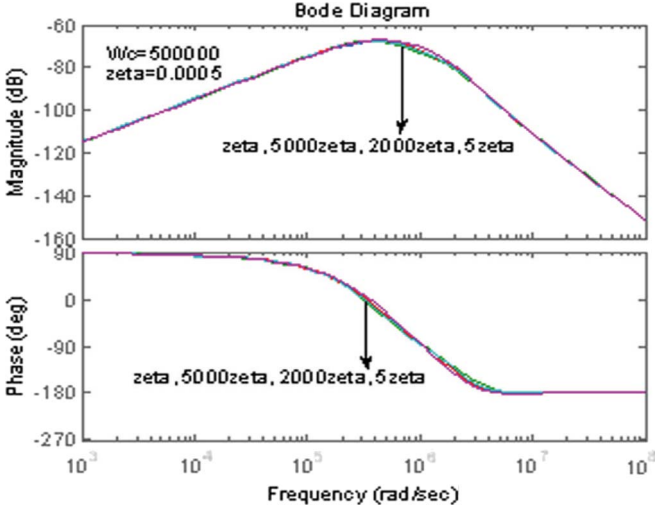


Fig. 4. Bode plots of $G_d(s)$ with different ζ 's.

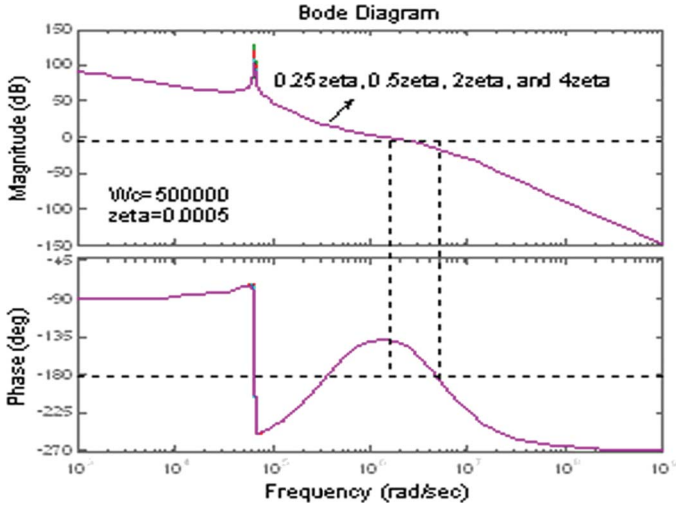


Fig. 5. Bode plots of $G_o(s)$ with different ζ 's.

frequency ω converges to zero or infinity, the $G_d(j\omega)$ will go to zero. This suggests that the disturbance will be attenuated to zero with the increase of system bandwidth. The Bode plots of (30) are shown in Figs. 3 and 4, in which the natural frequency ω_n and the damping coefficient ζ (zeta in Fig. 4) of the vibrational beam gyroscope are varying. The two figures demonstrated a desirable disturbance rejection property which is constant with the variations of the system parameters.

4) *Robustness and Stability Margin*: The bode diagrams of the loop gain TF given by (25) with varying damping coefficients and natural frequencies are shown in Figs. 5 and 6. The gain and phase margins of the system with variant damping coefficient are shown in Table II.

As the natural frequency is changing from $0.25 \omega_n$ to $4 \omega_n$, the stability margins of the system are exactly the same as the ones listed in Table II. From Figs. 5 and 6 and Table II, we can see that the ADRC is very robust against the parameter variations of the vibrational gyroscope, and the closed-loop control system is stable with reasonably large stability margins for the chosen $\omega_c (5 \times 10^5)$ and $\omega_o (\omega_o = 5 \omega_c)$.

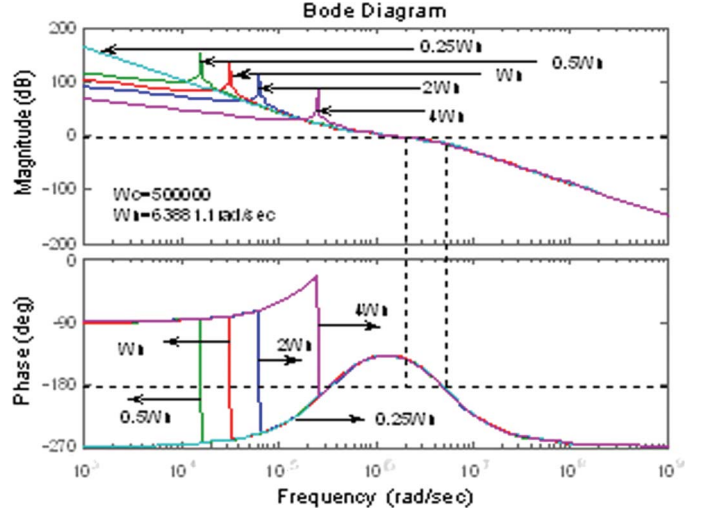


Fig. 6. Bode plots of $G_o(s)$ for different ω_n 's.

TABLE II
STABILITY MARGINS WITH DIFFERENT ζ 'S

Damping Coefficient	Gain Margin (dB)	Phase Margin
$\zeta=0.0005$	14.1773	41.2340
0.25ζ	14.1773	41.2320
0.5ζ	14.1773	41.2327
2ζ	14.1776	41.2367
4ζ	14.1779	41.2421

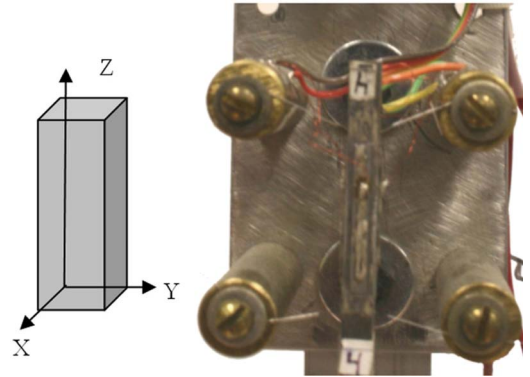


Fig. 7. Photograph of a piezoelectric beam gyroscope.

IV. SIMULATION RESULTS

Both of the simulation and hardware implementations of the ADRC are conducted on the vibrational beam gyroscope, whose photo is shown in Fig. 7. The gyroscope is composed of a steel beam (20 mm long) and four piezoelectric strips attached to each side of the beam as actuators and sensors. The controller will excite one of the bending modes of the beam gyroscope to make it oscillate at maximum magnitude and resonance frequency. As shown in Fig. 7, the rotation axis (Z) is along the length of the beam, and the drive (X) and sense (Y) axes are in the cross-sectional plane of the beam. The displacement output of the drive axis is a voltage level. Since the maximum magnitude of the output of the beam gyroscope is 100 mV, we

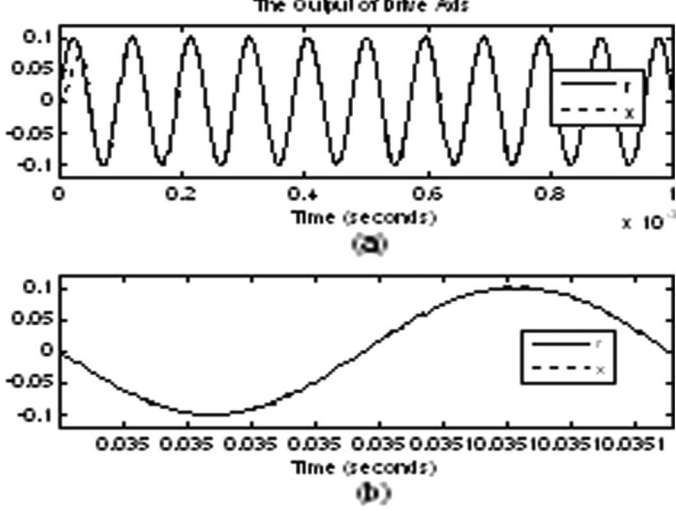


Fig. 8. Output x and the reference r .

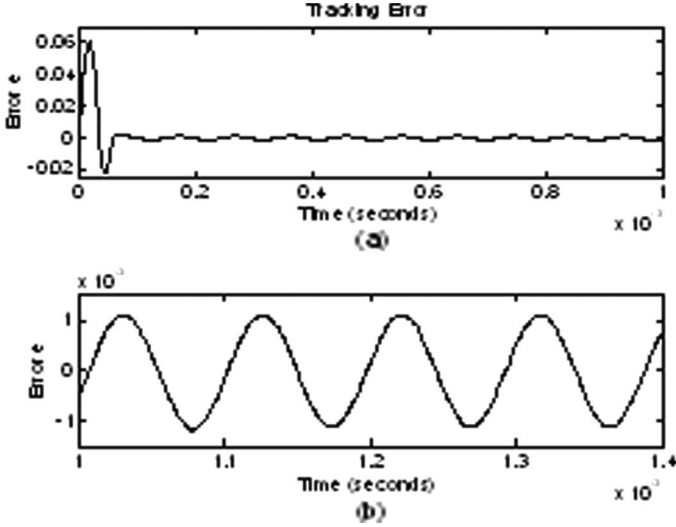


Fig. 9. Tracking error e of the drive axis.

take 0.1 in simulation unit to depict this. Then, the reference signal $r = 0.1 \sin(\omega t)$. The PSD of mechanical-thermal noise is $4.22 \times 10^{-26} \text{ N}^2 \cdot \text{s}$ according to [21]. We assume that the magnitude of the quadrature error term is 0.1% of the natural frequency as in [14]. The rotation rate is assumed to be constant, and $\Omega = 0.1 \text{ rad/s}$. About the ADRC and ESO, we choose ω_c as 5×10^5 and $\omega_o = 5 \omega_c$ as given before. The drive-mode controller is represented by

$$u_x = -\frac{1}{b}\hat{x}_3 + \frac{\omega_c^2}{b}(r - \hat{x}_1) + \frac{2\omega_c}{b}(\dot{r} - \hat{x}_2) + \ddot{r} \quad (31)$$

where ω_c and ω_c^2 , divided by constant b , are vastly reduced. Fig. 8(a) shows that the actual output x of the drive axis converges to the reference signal r very well after initial oscillation. Fig. 8(b) shows the output x and the r in one period which is around 0.1 ms as we desired. Fig. 9 shows the tracking error between the r and the x in different time ranges. The stabilized peak error is around 0.7% of the desired amplitude of the output x .

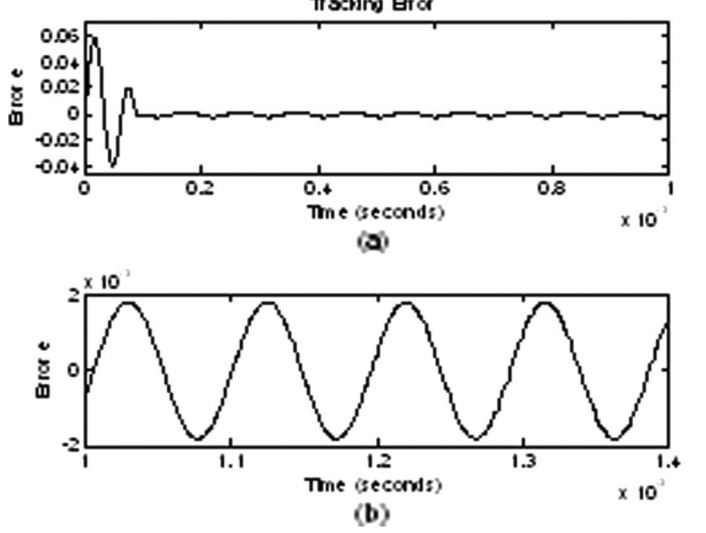


Fig. 10. Error e with 20% variations of ω_n and $\omega_{xy}y$.

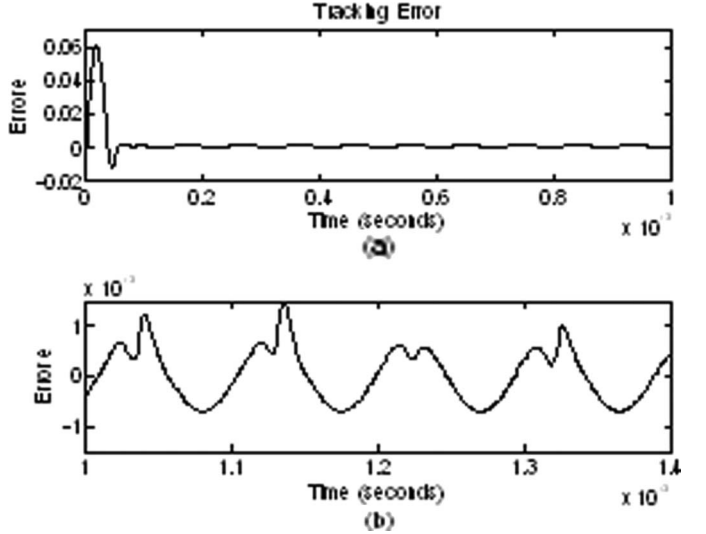


Fig. 11. Tracking error e with 30% variation of ζ .

Fig. 10 shows the tracking error e in different time ranges as there are 20% variations of ω_n and the magnitude of quadrature error term. The stabilized peak error is around 1.7% of the desired amplitude of x . The error is only a bit bigger than the one without variations. Fig. 11 shows the error e as there is 30% variation of the damping coefficient. The stabilized peak error of the error e is around 1.5% of the desired amplitude of x . As we increase the PSD of the mechanical-thermal noise in the simulation from $4.22 \times 10^{-26} \text{ N}^2 \cdot \text{s}$ to $4.22 \times 10^{-8} \text{ N}^2 \cdot \text{s}$, the output x is the same as the one in Fig. 8. The simulation results demonstrate the effectiveness and feasibility of the drive-mode controller u_x in the presences of parameter variations (within 40%) and the mechanical-thermal noise.

V. ANALOG IMPLEMENTATION AND EXPERIMENTAL RESULTS

The TFR of the ADRC is implemented onto the beam gyroscope using a field-programmable analog array (FPGA), which employs switched capacitor technology to model and construct

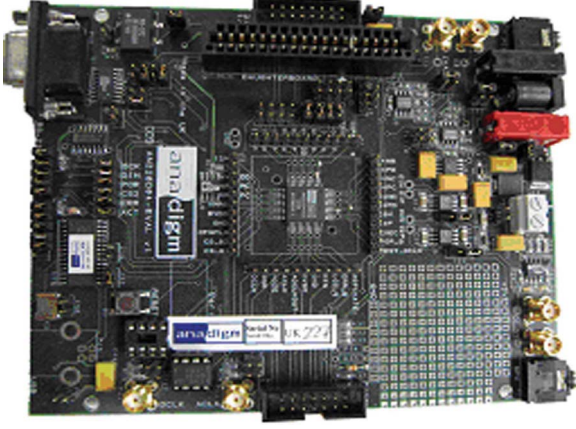


Fig. 12. FPAA board for analog implementation.

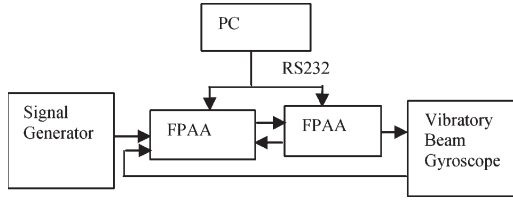


Fig. 13. Setup diagram of analog implementation of ADRC.

analog circuits. The FPAA-based analog implementation owns the advantages of fast response and low cost over the field-programmable-gate-array-based digital implementation [19], [20]. The design of the circuit is completed by a special software package and, then, is downloaded onto an FPAA chip. In our design, an AN221E04 FPAA chip (Fig. 12) is utilized, and the circuit design is accomplished through AnadigmDesigner2 software. The AN221E04 device consists of fully configurable analog blocks (CABs) and programmable resources. Configuration data are stored in an on-chip static random access memory. The CAB can be taken as a library of prebuilt configurable analog modules (CAMs), which are circuit blocks that approximate the true functionality of an analog part. Each CAM can be configured and wired to a desired functionality through an AnadigmDesigner2 user interface. Instead of choosing components (resistors, capacitors, etc.), the FPAA design is completed at a block diagram level. Hence, the CAMs have the same functionality as the blocks in Fig. 1. Since the FPAA is programmable, it greatly simplifies the circuit design. It also gives the flexibility to the overall control system because any changes of the system can be realized by reprogramming. Two FPAA boards are used in the experiment to implement the $H(s)$ and $G_c(s)$ in (24), respectively. The design was downloaded from a PC to the FPAA boards through RS232 connection. The setup diagram of the FPAA-based implementation is shown in Fig. 13, where the signal generator is applied to generate the reference signal r . We choose 100 mV as the desired amplitude of the reference signal. The other parameters of the beam gyroscope are subject to the variations of $\pm 10\%$ in the original values in practice.

The reference signal and the real output of the drive axis are shown in Fig. 14. The tracking error e between the real output of the drive axis and the reference signal is shown in

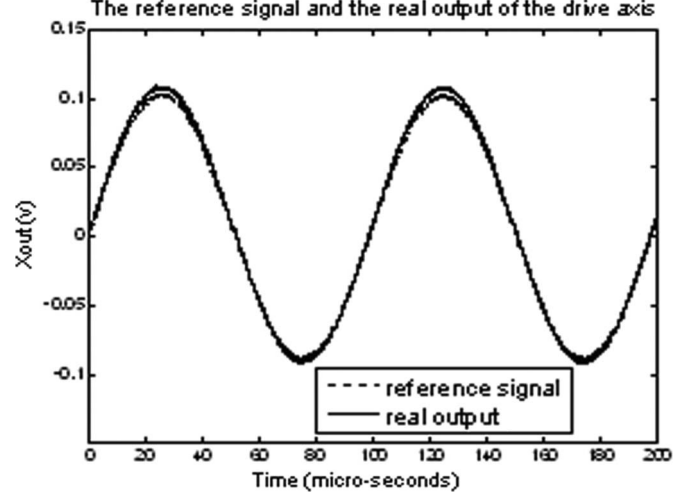


Fig. 14. Output of the drive axis (x) and reference signal (r).

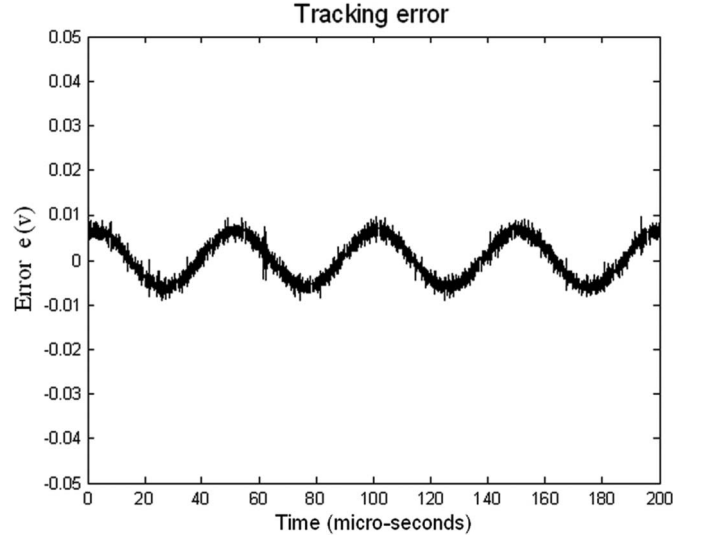


Fig. 15. Tracking error e between r and x .

Fig. 15. The peak error is about 10% of the original amplitude, which is bigger than the one in simulation. As we increase the observer gain (ω_o) by 30%, the peak error is still unchanged. Therefore, we believe that this is mainly caused by the feed-through noise in the switched capacitor circuitry of the FPAA board. The control signal is shown in Fig. 16. The experimental results further confirmed the effectiveness of the ADRC on the vibrational gyroscope.

VI. CONCLUDING REMARKS

We applied the ADRC to control the driving mode of MEMS gyroscopes. The controller is unique in two aspects. One is that the ADRC is very robust against structural uncertainties and extraneous disturbances of the MEMS gyroscopes. The other is that the two-parameter tuning feature makes the ADRC very practical and easy to implement in real world. The frequency-domain analysis proves that the tracking error of the drive axis is greatly decreased with the increase of the controller bandwidth. It also proves that, for a specific controller bandwidth, the closed-loop control system is not only stable with

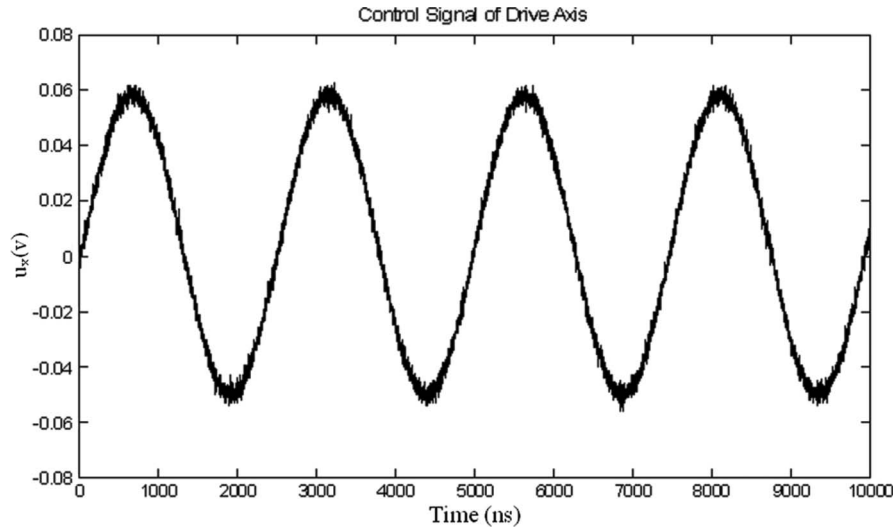


Fig. 16. Control input (u_x) to the drive axis.

large stability gains but also robust against parameter variations. The ADRC is successfully simulated and implemented on a vibrational beam gyroscope. The simulation and experimental results demonstrated an accurate tracking of the drive-axis output to the desired signal in the presences of parameter variations, noise, and quadrature errors, therefore verifying the effectiveness of the drive-mode controller.

REFERENCES

- [1] J. A. Geen, S. J. Sherman, J. F. Chang, and S. R. Lewis, "Single-chip surface micromachined integrated gyroscope with $50^\circ/\text{h}$ Allan deviation," *IEEE J. Solid-State Circuits*, vol. 37, no. 12, pp. 1860–1866, Dec. 2002.
- [2] N. Barbour and G. Schmidt, "Inertial sensor technology trends," *IEEE Sensors J.*, vol. 1, no. 4, pp. 332–339, Dec. 2001.
- [3] Y. Yazdi, F. Ayazi, and K. Najafi, "Micromachined inertial sensors," *Proc. IEEE*, vol. 86, no. 8, pp. 1640–1659, Aug. 1998.
- [4] R. T. M'Closkey, S. Gibson, and J. Hui, "Modal parameter identification of a MEMS gyroscope," in *Proc. Amer. Control Conf.*, Chicago, IL, Jun. 2000, pp. 1699–1704.
- [5] R. T. M'Closkey, S. Gibson, and J. Hui, "Input-output dynamics of the JPL microgyroscope," in *Proc. 37th IEEE Conf. Decision Control*, Dec. 1998, vol. 4, pp. 4328–4333.
- [6] Y. C. Chen, J. Hui, and R. T. M'Closkey, "Closed-loop identification of a micro-sensor," in *Proc. 42nd IEEE Conf. Decision Control*, 2003, vol. 3, pp. 2632–2637.
- [7] C. Acar and A. M. Shkel, "An approach for increasing drive-mode bandwidth of MEMS vibratory gyroscopes," *J. Microelectromech. Syst.*, vol. 14, no. 3, pp. 520–528, Jun. 2005.
- [8] R. T. M'Closkey and A. Vakakis, "Analysis of a microsensor automatic gain control loop," in *Proc. Am. Control Conf.*, San Diego, CA, Jun. 1999, pp. 3307–3311.
- [9] R. P. Leland, "Adaptive mode tuning for vibrational gyroscopes," *IEEE Trans. Control Syst. Technol.*, vol. 11, no. 2, pp. 242–247, Mar. 2003.
- [10] R. P. Leland, Y. Lipkin, and A. Highsmith, "Adaptive oscillator control for a vibrational gyroscope," in *Proc. Amer. Control Conf.*, Denver, CO, Jun. 2003, pp. 3347–3352.
- [11] R. Leland, "Adaptive control of a MEMS gyroscope using Lyapunov methods," *IEEE Trans. Control Syst. Technol.*, vol. 14, no. 2, pp. 278–283, Mar. 2006.
- [12] L. Dong and R. P. Leland, "The adaptive control system of a MEMS gyroscope with time-varying rotation rate," in *Proc. Amer. Control Conf.*, Portland, OR, Jun. 2005, pp. 3592–3597.
- [13] M. Salah, M. McIntyre, D. Dawson, and J. Wagner, "Time-varying angular rate sensing for a MEMS Z-axis gyroscope," in *Proc. 45th IEEE Conf. Decision Control*, Dec. 13–15, 2006, pp. 2165–2170.
- [14] S. Park and R. Horowitz, "New adaptive mode of operation for MEMS gyroscopes," *Trans. ASME, J. Dyn. Syst. Meas. Control*, vol. 126, no. 4, pp. 800–810, Dec. 2004.
- [15] D. Sun, "Comments on active disturbance rejection control," *IEEE Trans. Ind. Electron.*, vol. 54, no. 6, pp. 3428–3429, Dec. 2007.
- [16] Z. Gao, "Scaling and bandwidth-parameterization based controller tuning," in *Proc. Amer. Control Conf.*, Denver, CO, Jun. 2003, vol. 6, pp. 4989–4996.
- [17] Z. Gao, T. Trautzsch, and J. Dawson, "A stable self-tuning fuzzy logic control system for industrial temperature regulation," *IEEE Trans. Ind. Appl.*, vol. 38, no. 2, pp. 414–424, Mar./Apr. 2002.
- [18] S. Parvez and Z. Gao, "A wavelet-based multiresolution PID controller," *IEEE Trans. Ind. Appl.*, vol. 41, no. 2, pp. 537–543, Apr. 2002.
- [19] B. Sun and Z. Gao, "A DSP-based active disturbance rejection control design for a 1-kW H-bridge DC–DC power converter," *IEEE Trans. Ind. Electron.*, vol. 52, no. 5, pp. 1271–1277, Oct. 2005.
- [20] Z. Ping, "A hardware-reconfigurable control platform for space power management and distribution systems," Ph.D. dissertation, Cleveland State Univ., Cleveland, OH, 2005.
- [21] R. P. Leland, "Mechanical-thermal noise in MEMS gyroscopes," *IEEE Sensors J.*, vol. 5, no. 3, pp. 493–500, Jun. 2005.